The Characterization of the Dust Content in the Ring Around Sz 91: Indications of Planetesimal Formation?

Karina Maucó[1,2] , Carlos Carrasco-González[3] , Matthias R. Schreiber[2,4] , Anibal Sierra[5] , Johan Olofsson[1,2] ,
Amelia Bayo[1,2] , Claudio Caceres[6,7] , Hector Canovas[8] , and Aina Palau[3]

[1] Instituto de Física y Astronomía, Facultad de Ciencias, Universidad de Valparaíso, Av. Gran Bretaña 1111, 5030 Casilla, Valparaíso, Chile; karina.mauco@uv.cl
[2] Núcleo Milenio de Formación Planetaria—NPF, Universidad de Valparaíso, Av. Gran Bretaña 1111, Valparaíso, Chile
[3] Instituto de Radioastronomía y Astrofísica—IRyA, Universidad Nacional Autónoma de México, UNAM, campus Morelia, Antigua carretera a Pátzcuaro N°. 8701.
Col. Ex Hacienda San José de la Huerta, Morelia, Michoacán, C.P. 58089, México
[4] Universidad Técnica Federico Santa María, UTFSM, Avda. España 1680, Valparaíso, Chile
[5] Universidad de Chile, Departamento de Astronomía, Camino El Observatorio 1515, Las Condes, Santiago, Chile
[6] Departamento de Ciencias Fisicas, Facultad de Ciencias Exactas, Universidad Andres Bello, Av. Fernandez Concha 700, Las Condes, Santiago, Chile
[7] Núcleo Milenio Formación Planetaria—NPF, Universidad de Valparaíso, Av. Gran Bretaña 1111, Valparaíso, Chile
[8] Telespazio UK for the European Space Agency (ESA), European Space Astronomy Centre (ESAC), Camino Bajo del Castillo s/n, E-28692 Villanueva de la
Cañada, Madrid, Spain

Abstract

One of the most important questions in the field of planet formation is how millimeter- and centimeter-sized dust particles overcome radial drift and fragmentation barriers to form kilometer-sized planetesimals. ALMA observations of protoplanetary disks, in particular transition disks or disks with clear signs of substructures, can provide new constraints on theories of grain growth and planetesimal formation, and therefore represent one possibility for progress on this issue. We here present ALMA band 4 (2.1 mm) observations of the transition disk system Sz 91, and combine them with previously obtained band 6 (1.3 mm) and band 7 (0.9 mm) observations. Sz 91, with its well-defined millimeter ring, more extended gas disk, and evidence of smaller dust particles close to the star, constitutes a clear case of dust filtering and the accumulation of millimeter-sized particles in a gas pressure bump. We compute the spectral index (nearly constant at ∼3.34), optical depth (marginally optically thick), and maximum grain size (∼0.61 mm) in the dust ring from the multi-wavelength ALMA observations, and compare the results with recently published simulations of grain growth in disk substructures. Our observational results are in strong agreement with the predictions of models for grain growth in dust rings that include fragmentation and planetesimal formation through streaming instability.

Unified Astronomy Thesaurus concepts: Protoplanetary disks (1300); T Tauri stars (1681); Planetary-disk interactions (2204); Submillimeter astronomy (1647); Radio continuum emission (1340); Planet formation (1241); Planetesimals (1259)

1. Introduction

The most critical step in our understanding of the formation of terrestrial planets and giant planet cores is the assembly of kilometer-sized planetesimals from smaller dust particles (e.g., Johansen et al. 2014). The key problem is that the predicted short radial drift timescales for millimeter-/centimeter-sized particles when they decouple from the subKeplerian gas flow strongly limits the possibility of these particles growing into planetesimals (Weidenschilling 1977). The fact that planets exist and millimeter-sized dust particles are routinely observed at distances of ∼10−100 au from the host star (e.g., Barenfeld et al. 2017; Ansdell et al. 2018; Long et al. 2019; Cieza et al. 2021; Tazzari et al. 2021) clearly shows that the predicted fast inward migration of these solids is suppressed in most disks.

A crucial assumption leading to the predicted inward drift is that the gas pressure in the disk continuously decreases with the radius. Recent high-resolution ALMA observations of protoplanetary disks indicate that this assumption is most likely not generally correct. The groundbreaking image of the HL Tau disk (Partnership et al. 2015) and the results of the Disk Substructures at High Angular Resolution Project (DSHARP) program (Andrews et al. 2018) revealed that ringlike dust substructures are ubiquitous in relatively young protoplanetary disks. These findings are complemented by the identification of transition disks that show dense dust rings around dust-depleted cavities (e.g., Andrews et al. 2011; Pinilla et al. 2018; van der Marel et al. 2018). In several cases, these ringlike structures are accompanied by azimuthal asymmetries (e.g., Casassus et al. 2013; van der Marel et al. 2021), spiral arms (e.g., Christiaens et al. 2014; Huang et al. 2018a), or small and possibly inclined inner disks deduced from NIR observations (e.g., Marino et al. 2015) or using ALMA data (e.g., Pérez et al. 2018; Francis & van der Marel 2020).

One explanation for the observed ringlike substructures is that dust accumulates at local gas pressure maximums. These substructures in the gas pressure distribution may solve the drift and planetesimal formation timescale problems. For the origin of these pressure bumps in transition disks, embedded planets or companions (e.g., Zhu et al. 2011), dead zones (e.g., Flock et al. 2015), and/or internal photoevaporation (Alexander & Armitage 2007) have been suggested. Photoevaporation alone is generally ruled out by the high accretion rates found in most transition disks (Owen & Clarke 2012), and dead zones alone fail to explain deep observed gas gaps (Pinilla et al. 2016). Planet–disk interactions are particularly favored, as they can explain some of the main features observed in most systems: the differences in radii between the gas and the dust component, and also between dust grains of different sizes (e.g., Garufi et al. 2013; van der Marel et al. 2016; Dong et al. 2017), for instance. If Jupiter-like

planets are responsible for the pressure bump, then the small particles will leak into the cavity, reaching the inner regions (e.g., Pinilla et al. 2016). This allows for the presence of inner disks over million-year timescales (e.g., Pinilla et al. 2021). In any case, the millimeter-/centimeter-sized particles that are trapped in the pressure bump may have enough time to agglomerate and form planetesimals.

Grain growth significantly affects the optical properties of dust particles. At millimeter wavelengths, the slope of the spectral energy distribution, i.e., the spectral index, has been widely used to estimate the maximum grain size of dust grains (e.g., Williams & Cieza 2011). Several observational studies have now provided strong evidence for grain growth in disks (e.g., Calvet et al. 2002; Testi et al. 2003; Natta et al. 2004; Pérez et al. 2012; Tsukagoshi et al. 2016; Carrasco-González et al. 2019). These observational results have recently been complemented with simulations of grain growth in a dust ring (Stammler et al. 2019), including fragmentation and planetesimal formation. According to these models, given the self-regulating nature of planetesimal formation, which stabilizes the midplane dust-to-gas ratio, once fragmentation sets in, the spectral index in the ring is predicted to reach its minimum value. Furthermore, in line with the idea that planetesimal formation may take place in ringlike substructures, the simulations show that planetesimal formation can naturally explain the surprisingly similar optical depths derived for the rings of the DSHARP targets (Dullemond et al. 2018; Huang et al. 2018b). However, given the still small number of targets observed at high resolution, it cannot be excluded that the derived optical depths cluster in the range of 0.2-0.6 by coincidence (Stammler et al. 2019). Moreover, it remains to be tested whether the ringlike accumulations around the dust-depleted cavities in transition disks show similar characteristics to the substructures of the DSHARP disks. Thus, additional high-resolution observations of ring structures are greatly required. In this regard, Sz 91 represents an ideal complementary target to the DSHARP sample.

Sz 91 is a 3–5 Myr old T Tauri star of spectral type M0 located in the Lupus III molecular cloud (Romero et al. 2012; Canovas et al. 2015), at a distance of 159 ± 2 pc (Gaia Early Data Release 3 (EDR3); Gaia Collaboration et al. 2016, 2012), accreting from a transition disk at a rate of $\dot{M} \sim 10^{-8.8} M_{\odot} \, yr^{-1}$ (Alcalá et al. 2017). High angular resolution ALMA band 7 observations revealed that the millimeter-sized dust particles are concentrated in a ringlike structure (Canovas et al. 2016) extending from 86 to 101 au (Francis & van der Marel 2020), while the polarized light observations are best explained by small, porous grains distributed in a disk with a significantly smaller (~45 au) cavity (Maucó et al. 2020). The gas component of the disk extends from inside the millimeter cavity, with a gas-depleted cavity at 37 au (van der Marel et al. 2021), up to $\sim$ 400 au from the star (Tsukagoshi et al. 2019). Such a disk structure, with an extended gas disk, a concentration of millimeter-sized particles in a well-defined ringlike structure, and smaller dust particles inside the millimeter cavity, is indicative of the radial drift of the millimeter-sized dust particles that decoupled from the gas flow and the presence of a local pressure maximum that acts as a dust filter. This filter halts the radial drift of the millimeter-/centimeter-sized particles, while the smaller dust particles pass the pressure maximum (e.g., Rice et al. 2006).

Here we present new ALMA band 4 (2.1 mm) observations of the transition disk Sz 91, and combine them with the archival band 6 (1.3 mm) and band 7 (0.9 mm) data to constrain the optical depth, the dust surface density, and the grain size distribution of the dust particles that are trapped in the ring, by performing a radial analysis of the ALMA spectral energy distribution (SED), including optical depth and scattering effects. Comparing our results with the predictions of theoretical models of grain growth in ringlike substructures that include planetesimal formation (Stammler et al. 2019), we find excellent agreement with our observational results, which may indicate that planetesimal formation is occurring in the millimeter dust ring around Sz 91.

2. Observations and Data Reduction

With the aim of characterizing the dust content in the ring around Sz 91, we analyzed new 2.1 mm ALMA data (band 4), as well as archival 1.3 mm (band 6) and 0.9 mm (band 7) data.

2.1. Band 4 Observations

We obtained 2.1 mm observations of Sz 91 (project ID 2018.1.01020.S) by combining ALMA 12-m array extended (C43-8) and more compact (C43-5) configurations, resulting in baselines ranging from 15 m to 8.55 km and a total of 43-48 antennas. The combined observations are sensitive to spatial scales of up to $17''$. The long baseline observations were acquired in three different blocks of ~50 minutes each (2.15 h in total) on 2019 July 22, 23, and 28 (cycle 6). The short baseline observations were executed in two different blocks of ~40 minutes each (~1.3 h in total) on 2018 November 11 and 22.

The precipitable water vapor ranged between 0.5 and 2.0 mm. The observations of the phase calibrator (J1610-3958) were alternated with the science observations to calibrate the time-dependent variation of the complex gains. The cycling times for the phase calibration were set to 8 minutes and to 54 s for the compact and extended configurations, respectively. The ALMA correlator was configured in Frequency Division Mode. The band 4 receiver system was employed to detect the continuum emission at band 4 (146.40 GHz), and four spectral windows with 1.875 GHz bandwidth were set up to detect the dust continuum, centered at 132.4, 134.35, 144.46, and 146.40 GHz, respectively. We set the frequency of the last spectral window to aim for the possible detection of the CS $v = 0$ $J = 3–2$ spectral line at 146.9690 GHz, with a channel spacing of 976.562 kHz, which corresponds to a velocity resolution of $\sim 2.0 \, km \, s^{-1}$.

The visibility data were reduced and calibrated using the Common Astronomical Software Application package (CASA; McMullin et al. 2007). The raw data were calibrated with the reduction script provided by the ALMA staff—Pipeline version 42030M (Pipeline-CASA54-P1-B), which includes offline Water Vapor Radiometer calibration, system temperature correction, and bandpass, phase, and amplitude calibrations. The short baseline and long baseline data sets were calibrated independently. We shifted the phase center of the visibilities of the compact configuration to the position of Sz 91 at the date of the long baseline observations, as determined from the position and proper motions of the source $(-10.0, -22.8)$ mas yr^{-1} reported by Gaia EDR3 (Gaia Collaboration et al. 2016, 2012), using the task fixvis in CASA.

The image reconstruction was performed with the CLEAN algorithm (CASA version 5.6.2-2, task tclean), using Briggs weighting with a robust parameter of 0.5. The final continuum image has a peak of 70 μJy beam^{-1} and an rms of 5 μJy beam^{-1} for a synthesized beam of 103×91 mas. Integrating

Table 1
ALMA Images Used to Estimate the Spectral Indices

Band	Wavelength (mm)	Frequency (GHz)	Maximum Intensity (mJy beam^{-1})	Flux (mJy)	SNR	rms Noise (mJy beam^{-1})	Resolution (mas)	Method
B7	0.9	349.4	4.0	44.0	∼33	1.0	220	Radial profiles
B6	1.3	225.0	0.76	13.0	∼7	0.3	220	Radial profiles
B4	2.1	139.4	0.16	2.1	∼20	0.05	220	Radial profiles
B7	0.9	349.4	2.22	44.6	∼23	0.6	150	CASA task `immath`
B4	2.1	139.4	0.10	2.1	∼17	0.02	150	CASA task `immath`

Note. The band 6 continuum data was completely flagged in the raw data set due to problems with the correlator.

the flux inside an elliptical region enclosing the totality of the source with semimajor axis $a = 1''03$ and semiminor axis $b = 0''93$ results in $F_{2.1\,mm} = 2.3 \pm 0.1$ mJy. We also obtained a continuum image at 220 mas resolution (see Section 2.2), peaking at 0.16 mJy beam^{-1} and with an rms of 0.05 μJy beam^{-1}. As before, the integrated flux inside the same elliptical region results in $F_{2.1\,mm} = 2.1 \pm 0.1$ mJy. The integrated flux errors include the absolute flux calibration error of 5%, which dominates the uncertainty.

The visibilities of the line emission, on the other hand, were obtained by subtracting the continuum visibilities with velocity steps of 2.0 km s^{-1}. The CLEAN image was obtained using a natural weighting and has a beam size of 197×180 mas with an rms noise level of 0.32 mJy beam^{-1}. The CS v = 0 J = 3–2 line detection is discussed in Appendix B.

2.2. Archival Data

We used archive ALMA continuum images of Sz 91 at band 7 (project ID 2012.1.00761.S) and band 6 (project ID 2015.1.01301.S) to complement our study in order to estimate the spectral indices. For this, we obtained CLEAN images by following the same methodology and parameters as for our band 4 observations. Table 1 lists the characteristics of the final ALMA images used in this work.

To compare images at different wavelengths, they must be at the same angular resolution. Given that the weighting of the visibilities affects the sensitivity and angular resolution of the final images (as greater weighting to longer baselines implies worse sensitivity), we compared the beam sizes and rms noises obtained for different weightings at different bands, and concluded that the best compromise between resolution and sensitivity was obtained by using a Briggs weighting with a robust parameter of 0.5 and convolving all images to a circular beam with a diameter of 220 mas, equivalent to a physical size of ∼35 au, at the distance of Sz 91 ($d = 159 \pm 2$ pc). Then we obtained the corresponding CLEAN images at each wavelength with angular resolutions of 220 mas or less (see Table 1) and convolved them using the task `imsmooth` in CASA.

The final band 7 image peaks at 4.0 mJy beam^{-1} and has an rms of 1.0 mJy beam^{-1}, and the band 6 image reaches 0.76 mJy beam^{-1} and has an rms of 0.3 mJy beam^{-1}, both for a circular synthesized beam of 220 mas. We remark, however, that the whole continuum windows for the band 6 data set were flagged due to problems with the correlator. Therefore, we only used the line-free channels of the spectral windows assigned for line detection to create the image. This is the reason for its low peak intensity. The synthesized beam of 220 mas was basically set by this (noisy) data set. Integrating the flux inside the same region used for the B4 images results in $F_{0.9\,mm} = 44 \pm 4$ mJy
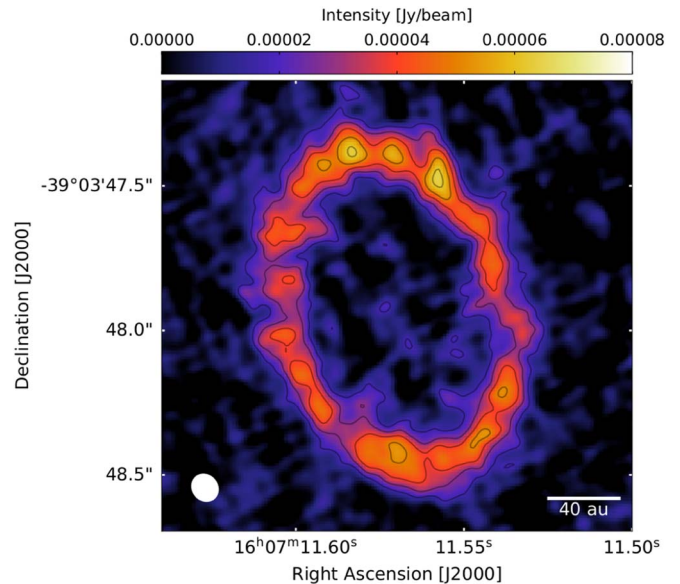

Figure 1. ALMA continuum observations at 2.1 mm (band 4) of the disk around Sz 91. The beam size was 103×91 mas (16.4×14.5 au), and is shown in the bottom left of the image. The contour levels correspond to 3, 5, 7, 9, and 11σ, where σ is the image rms.

and $F_{1.3\,mm} = 13.0 \pm 0.6$ mJy. These values include the absolute flux calibration error at each frequency. For this, we used the nominal values of 10% at band 7 and 5% at band 6. We remark that the integrated flux errors obtained here are dominated by flux calibration errors.

3. Results

3.1. Continuum Emission and Radial Profiles

Figure 1 shows the 2.1 mm (band 4) ALMA continuum image of Sz 91. We clearly resolved the disk ring structure, with the north side being brighter than the south side (a peak-to-peak ratio of 1.15), something also found in the ALMA observations at 0.9 mm in Tsukagoshi et al. (2019). Unfortunately, given the current resolution of our data, we could only partially resolve the ring in the radial direction.

We estimated the radial profiles of the dust emission at different wavelengths by averaging the emission in concentric elliptical rings with widths of 15 mas, using an eccentricity given by the disk inclination (49°7) and position (18°1) angles taken from the ALMA band 7 continuum image from Tsukagoshi et al. (2019). The intensity at each radius was given by the azimuthally averaged intensity in the ring, and the errors were calculated as $\Delta I_\nu = \mathrm{rms}_\nu / (\Omega_{ring}/\Omega_{beam})^{0.5}$, where Ω_{ring} and Ω_{beam} are the solid angles of the ring and the synthesized beam, respectively.
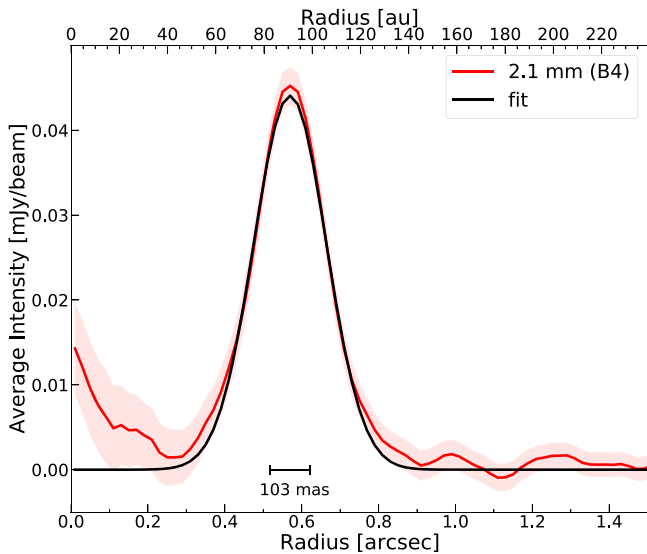
Figure 2. The radial profile (red line) after azimuthally averaging the deprojected continuum image shown in Figure 1 (assuming $d = 159$ pc) at 2.1 mm. Statistical errors (based on the rms noise of the map) at the 1σ level are shown as the filled band around the nominal value. A Gaussian fit to the profile is shown as a solid black line with an FWHM of $0''.21$ (33.4 au). The horizontal bar indicates the beam major axis for comparison.
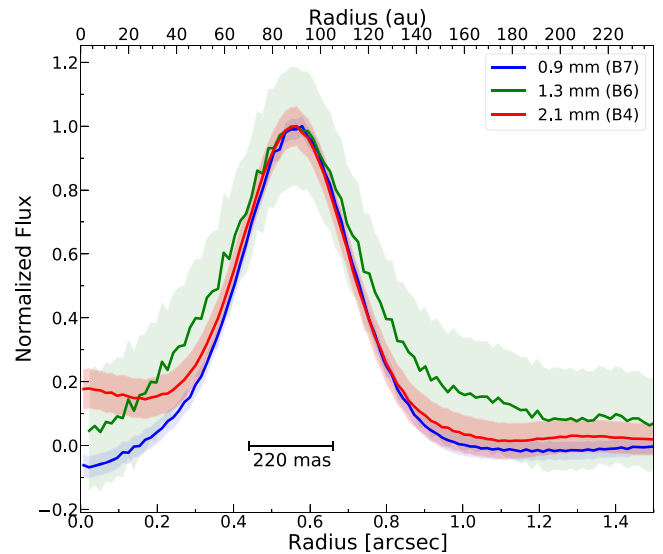

Figure 3. Normalized radial profiles of the three data sets used in this work (see Table 1), convolved to a circular beam of 220 mas (horizontal bar). Statistical errors (based on the rms noise of each map) at the 1σ level are shown as the filled bands around the nominal values in each case.

The brightness temperature profiles were calculated from the blackbody Planck function, without assuming the Rayleigh–Jeans regime, to avoid errors at short wavelengths in the outer parts of the disk, where dust temperatures are expected to be low. The profiles were calculated using the following relationship:

$$T_B = \frac{h\nu}{k_B \ln\left[1 + \frac{2h\nu^3}{I_\nu c^2}\right]}, \quad (1)$$

where h is the Planck constant; k_B is the Boltzmann constant; I_ν is the intensity at frequency ν; and c is the speed of light.

The radial profile of our band 4 observations is shown in Figure 2 (red line). Statistical errors (based on the rms noise of the map) at the 1σ level are shown as shaded regions around the nominal value. We fitted a Gaussian curve to the profile using the python module mpfit[9] (black line), with an FWHM of $0''.21$ (33.4 au). On the other hand, the normalized radial profiles of all three data sets used in this work for a circular synthesized beam of 220 mas (35 au) are shown in Figure 3. The peaks of the emissions are located $\sim$90 au from the central star in all the profiles.

We remark that even though we used a data set convolved to a resolution of 220 mas (where the disk was not radially resolved), this resolution was very similar to the actual width of the ring estimated from our highest angular resolution observations at band 4, as shown in Figure 2. In this sense, the estimate of the physical parameters reported in Section 3, despite being considered lower limits, should be very similar to the average values of the real disk parameters.

The integrated fluxes that we estimated at band 6 and band 7 for a resolution of 220 mas (Section 2.2) are consistent with the reported fluxes in the literature. Tsukagoshi et al. (2019) reported $F_{0.9\,\mathrm{mm}} = 45.2 \pm 0.5$ mJy, estimated inside the regions with S/N $> 3\sigma$. Note that the flux reported in Tsukagoshi et al. (2019) was

at a resolution of $\sim$130 mas, which agrees very well with the flux estimated from our band 7 image at 150 mas of $F_{0.9\,\mathrm{mm}} = 44.6 \pm 4.4$ mJy (see Table 1). On the other hand, our integrated flux at band 6 agrees very well with the one reported in Canovas et al. (2015), with a value of 12.7 ± 1.9 mJy.

Note the excess emission inward 40 au at 2.1 mm on Figure 3, also visible at a higher resolution in Figure 2. Moreover, the band 4 emission inside the ring of dust (r < 60 au) clearly exceeds the band 7 profile. Given that the excess is not present in the radial profiles of Tsukagoshi et al. (2019) at band 7, where the disk is expected to be brighter, especially at a lower resolution, we can conclude that the excess observed in our data represents a real detection.

Based on this detection and the nondetection in band 7, we can estimate an upper limit to the spectral index at the inner regions. We found an $\alpha_{2.1-0.9\,\mathrm{mm}}$ upper limit $\lesssim 2.8$. Even though this limit does not rule out the presence of an inner disk (dust thermal emission), the most probable explanation for it is free–free emission from ionized gas close to the central star. This could produce an increase in the 2.1 mm emission at the inner regions of the disk, which would result in an apparent excess. We are inclined to the free–free emission scenario, because the band 7 observations are more favorable for detecting an inner disk, as stated above. Also, there is no excess NIR emission in the SED of the source (Canovas et al. 2015). Given all these reasons, we can conclude that the excess observed in our data is more consistent with free–free emission. This type of emission has recently been detected at similar wavelengths in the TW Hydra disk (Macías et al. 2021), and it has been reported at 7 mm, 15 mm, and centimeter wavelengths in other disks as well (e.g., Ubach et al. 2012, 2017; Macías et al. 2018). Radio flux monitoring at multiple epochs and at different wavelengths will be needed in order to disentangle the physical mechanisms responsible for the excess emission at millimeter wavelengths in Sz 91 (Ubach et al. 2017).

As before, we fitted Gaussian curves to the intensity profiles using mpfit, and found FWHMs of $0''.353 \pm 0.007$ and $0''.329 \pm 0.004$ for the band 4 and band 7 profiles, respectively.
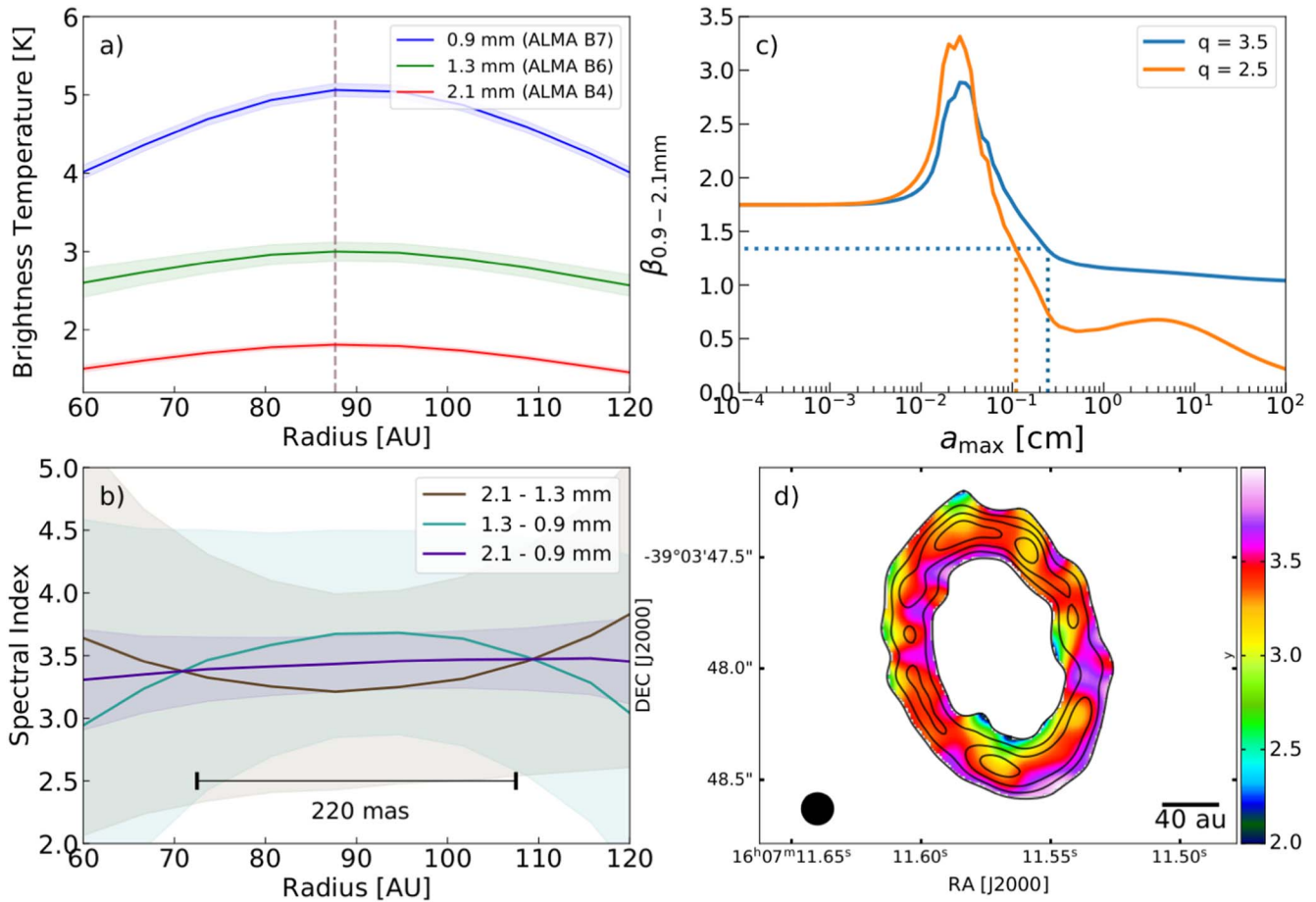
---

[9] https://github.com/segasai/astrolibpy/blob/master/mpfit/mpfit.py

Figure 4. (*a*): The radial profiles of the brightness temperatures in the ALMA images. Dashed lines indicate brightness temperature peak values (the same for all bands). (*b*): The spectral indices between different combinations of wavelengths. The spectral indices were computed using the radial profiles of Figure 3 (at 220 mas resolution). The spectral indices are only reliable from 60 to 120 au, where emission from the dusty disk is expected. Uncertainties at the 1σ level are shown as shaded regions. We obtained an average spectral index of $\alpha = 3.34 \pm 0.26$. (*c*): The slope of the dust opacity coefficient, β, from 0.9–2.1 mm, using the DSHARP opacities from Birnstiel et al. (2018) for a power-law index of the dust size distribution of $q = 3.5$ (blue) and $q = 2.5$ (orange). The horizontal dashed line indicates the value of $\beta = 1.34$ estimated for the disk around Sz 91 (assuming optically thin emission). We obtained $a_{\rm max}$ values of ∼2.5 mm and ∼1 mm for $q = 3.5$ and $q = 2.5$, respectively (the vertical dashed lines). (*d*): A spectral index map (at 5σ) between 2.1 and 0.9 mm, using the final continuum images listed at the bottom of Table 1 convolved to an angular resolution of 150 mas (23.8 au), and shown by the filled circle at the bottom left. Overlaid are the contours of the continuum image at 2.1 mm (band 4) from Figure 1 at the same resolution. The contour levels correspond to 5, 8, 11, and 14σ, where σ is the image rms. The spectral index has an average value of 3.37.

The slight difference was due to the excess emission in the band 4 profile, as mentioned before. Observations at higher angular resolutions and at longer wavelengths will be needed in order to investigate whether there is any variation in the width of the dust ring at different wavelengths, as expected from dust evolutionary models (Pinilla et al. 2015a; Powell et al. 2019), but as yet observationally undetected (e.g., Norfolk et al. 2021).

3.2. Spectral Indices and Brightness Temperatures

The millimeter spectral index between two different wavelengths, defined as $\alpha = \log(I_{\nu 1}/I_{\nu 2})/\log(\nu_1/\nu_2)$, has been widely used to study grain growth in protoplanetary disks (e.g., Williams & Cieza 2011).

We derived spectral indices based on the band 4, band 6, and band 7 ALMA data. Using the intensities observed at different wavelengths, taken from their respective radial profiles (at 220 mas resolution), we obtained the spectral indices by combining data at multiple bands: $\alpha(2.1$–$1.3\,{\rm mm})$, $\alpha(1.3$–$0.9\,{\rm mm})$, and $\alpha(2.1$–$0.9\,{\rm mm})$. Figure 4 shows the brightness temperatures (panel *a*) and spectral indices (panel *b*) estimated in this way. As shown in the figure, the spectral index throughout the disk region is

almost constant, with an average value of 3.34 ± 0.26. This result is consistent with the value of $\alpha_{0.8-2.7\,{\rm mm}} = 3.36$ as previously found by Canovas et al. (2015). The *x*-axis in panel *b* is shown from 60 to 120 au, since this is where the emission from the dusty ring is expected (see Figure 2). The $\alpha(2.1$–$0.9\,{\rm mm})$ index is the most reliable index, given its lower uncertainty level (the shaded region).

Based on this, and since the band 6 data set has the lowest SNR, we computed the spectral index map of $\alpha(2.1$–$0.9\,{\rm mm})$ by using the band 4 and 7 observations at a higher resolution. We used the CASA task `immath`, with the mode option *spix*. First, we constructed primary beam corrected images with a resolution of 150 mas (circular beam) using `imsmooth`, as before (the bottom part of Table 1). This resolution was set by the band 7 images. Then we aligned both data sets using the CASA task `UVfix`, where the band 7 visibilities were shifted in order to match those of the band 4 data set. For this, we used the source proper motions, which yielded offsets of $\Delta\alpha = 0\rlap.{''}04$ and $\Delta\delta = 0\rlap.{''}09$.

The result was a spectral index map, as shown in Figure 4 (panel *d*), to which we applied a filter in order to keep only the

pixels with emissions well above the noise level (5σ, 30 μJy beam^{-1}) of the band 4 continuum image (see Table 1). A clear trend of an increasing spectral index with radius (as expected from the grain growth and radial drift) was not found, nor were any azimuthal variations. However, we obtained a mean α value of 3.37, consistent with the α value estimated from the radial intensity profiles. Furthermore, the flat shape of the spectral index observed in panel b was also found when using the radial profiles of band 4 and band 7 at 150 mas. Higher resolution observations will be needed in order to resolve the disk in the radial direction, to be able to study the radial modulations of α.

Finally, the low brightness temperatures in Figure 4 seem to indicate that the emission is optically thin. In this regime, the brightness temperature is given by $T_B = T_d\, \tau_\nu$, where T_d is the dust temperature and τ_ν is the optical depth at frequency ν. Since τ_ν is <1 (i.e., optically thin), the T_B that we detected was lower than the real dust temperature at that location. The dust emission comes from regions located more than 60 au from the central star (see Figures 2 and 3), so low temperatures are expected at those large radii. Low brightness temperatures of roughly the same order (at similar radii) as the ones we found here have previously been found for similar objects (e.g., Pérez et al. 2015).

3.3. Maximum Grain Size and Optical Depth

Dust grains are the main source of opacity in disks. Consequently, the emission and absorption of radiation by dust grains produces the final disk spectrum. The spectral index has been widely used to estimate grain properties, particularly the maximum grain size, a_{max}, assuming that the emission from the disk is optically thin and that scattering can be neglected (e.g., Beckwith & Sargent 1991; Jørgensen et al. 2007). However, in an early work, Miyake & Nakagawa (1993) pointed out that the scattering coefficient is much larger than the absorption coefficient at millimeter wavelengths if the dust grains are millimeter/centimeter-sized, which is expected to be the case for protoplanetary disks. The importance of scattering at millimeter–centimeter wavelengths has recently been reinforced by other authors (Carrasco-González et al. 2019; Liu 2019; Sierra et al. 2019; Soon et al. 2017; Sierra & Lizano 2020). The general picture that is emerging is that the assumption of optically thin emission with negligible contributions from scattering are not generally justified, and that in order to use the spectral index to characterize dust grains, parameters such as dust opacity and scattering efficiency need to be taken into account.

In what follows, we estimate the maximum grain size in the ring around Sz 91 in two different ways. First, we follow the classical approach and assume that the disk is optically thin and that scattering can be neglected. We then complement this simple estimate by performing a radial analysis of the millimeter spectrum to simultaneously obtain the dust surface density, the optical depth, and the maximum particle size at each radius, without assuming any value of optical depth at any wavelength and including scattering effects.

3.3.1. Classical Approach

At millimeter wavelengths, the emission is within the Rayleigh–Jeans regime, so the emergent intensity is proportional to the Planck function, $B_\nu(T_d)$, which in turn behaves as $B_\nu(T_d) \propto \nu^2$. Also, at these longer wavelengths, the opacity

follows a power-law dependency on frequency. In the optically thin regime ($\tau_\nu \ll 1$), and in a pure absorption case, the total intensity can be written as $I_\nu \propto \nu^{2+\beta_{abs}}$, where β_{abs} is the slope of the absorption coefficient. Therefore, knowing the spectral slope $\alpha = 2 + \beta_{abs}$, i.e., the spectral index, allows the inference of the maximum grain size, a_{max}, from the spectral behavior of β_{abs} for different particle size distributions. The latter is typically assumed to be adequately described by a power-law of the form $n(a) \propto a^{-q}$, with a as the particle radius, and with slope $q = 3.5$, resembling the size distribution found in the Interstellar Medium (ISM). However, lower values of q are expected in protoplanetary disks, as grain growth acts in the system, building up millimeter–centimeter particles (Drążkowska et al. 2019). We therefore used, in addition to the canonical value ($q = 3.5$), a smaller exponent of $q = 2.5$. For these assumptions, and using the DSHARP opacities (Birnstiel et al. 2018), our spectral index value of $\alpha = 3.34$, as found in Section 3.2, will translate to $\beta_{abs} = 1.34$, which implies $a_{max} \sim 2.5$ and 1 mm for $q = 3.5$ and $q = 2.5$, respectively (panel c in Figure 4).

3.3.2. Radial Fitting

Given that protoplanetary disks can be optically thick, and that scattering can dominate the total emission, we complemented the simple estimate of the maximum particle size by using the approach described in detail in Carrasco-González et al. (2019). We performed a radial analysis of the millimeter spectrum by modeling the radial intensity profiles at each ALMA wavelength, assuming an axisymmetric, geometrically thin, and vertically isothermal disk. We also assumed a constant dust temperature along the line of sight. Since dust evolution models predict slightly flatter slopes for the particle size distribution at the position of dust rings (e.g., Drążkowska et al. 2019), we assumed $q = 3.0$ and adopted the dust composition used by the DSHARP program (Birnstiel et al. 2018). The millimeter spectrum at each radius was fitted using the dust continuum emission at 0.9, 1.3, and 2.1 mm, up to a radius where the observations at all bands had an SNR of at least 1.5. In our modeling, the dust scattering effects on the radiative transfer equation (Zhu et al. 2019) were taken into account. In particular, we used the solution found by Sierra et al. (2019), which was also used to fit the dust properties in the disk around HL Tau (Carrasco-González et al. 2019). According to Sierra et al. (2019), the emergent intensity at a particular radius can be written as:

$$I_\nu = B_\nu(T_d)[(1 - \exp(-\tau_\nu/\mu)) + \omega_\nu F(\tau_\nu, \omega_\nu)], \quad (2)$$

where $\tau_\nu = \Sigma_d \chi_\nu$ is the optical depth; Σ_d is the dust surface density; $\chi_\nu = \kappa_\nu + \sigma_\nu$ is the total dust opacity (i.e., the extinction coefficient), with κ_ν and σ_ν as the absorption and scattering coefficients, respectively; $\omega_\nu = \sigma_\nu/(\kappa_\nu + \sigma_\nu)$ is the dust albedo; $\mu = \cos(i)$ is the cosine of the inclination angle, i; and $F(\tau_\nu, \omega_\nu)$ is defined as:

$$F(\tau_\nu, \omega_\nu) = \frac{1}{\exp(-\sqrt{3}\,\epsilon_\nu \tau_\nu)(\epsilon_\nu - 1) - (\epsilon_\nu + 1)}$$
$$\times \left[\frac{1 - \exp(-(\sqrt{3}\,\epsilon_\nu + 1/\mu)\tau_\nu)}{\sqrt{3}\,\epsilon_\nu\mu + 1} \right.$$
$$\left. + \frac{\exp(-\tau_\nu/\mu) - \exp(-\sqrt{3}\,\epsilon_\nu \tau_\nu)}{\sqrt{3}\,\epsilon_\nu\mu - 1} \right], \quad (3)$$

where $\epsilon_\nu = \sqrt{1 - \omega_\nu}$. We also included anisotropic scattering by using, instead of σ_ν, an effective scattering coefficient defined as $\sigma_\nu^{\mathrm{eff}} = (1 - g_\nu)\sigma_\nu$, where g_ν is the asymmetry parameter. Given a particle size distribution (with $q = 3.0$) and grain composition (from the DSHARP program), Equation (2) depends on only three free parameters: T_d, Σ_d, $a_{\max}$. However, we fixed the dust temperature at each radius to the expected value for a passively irradiated flared disk in radiative equilibrium, following Equation (3) in Huang et al. 2018b. Therefore, our free parameters were only the dust surface density Σ_d and the maximum grain size $a_{\max}$. For our analysis, we varied Σ_d from $10^{-6.0}$ to 10 g cm^{-2} and $a_{\max}$ from $10^{-1.7}$ to 1 cm, both in logarithmic space with a total of 100 intervals.

The probability of each parameter (at each radius) was computed by comparing the observed intensities with the emergent intensities for different combinations of the free parameters. The probability P for each pair of free parameters was computed using a log-normal likelihood function:

$$P = \exp\left(-0.5 \sum_i \left(\frac{I_i - I_{m,i}}{\hat{\sigma}_{I,i}}\right)^2\right), \qquad (4)$$

where I_i is the azimuthally averaged intensity for a given radius and frequency; $I_{m,i}$ is the model intensity at the same radius and frequency; and $\hat{\sigma}_{I,i}$ is the uncertainty (also at the same radius) given by:

$$\hat{\sigma}_{I,i} = \sqrt{\sigma_{I,i}^2 + (\delta_i I_i)^2}, \qquad (5)$$

where $\sigma_{I,i}$ is the error of the mean computed from the azimuthally averaged intensity profiles; and δ_i is the absolute flux calibration error at each frequency. For this, we used the nominal values of 10% at band 7 and 5% at band 6 and band 4. A detailed description and discussion of this methodology is presented in Sierra & MAPS Team (2021). The radial profiles of the dust surface density and maximum grain size were constructed using the free parameters with the highest probability at each radius.

The optical depth profiles obtained for the ring around Sz 91 are shown in Figure 5. The red, green, and blue lines indicate the ALMA band 4, 6, and 7 optical depths, respectively. The dashed lines represent the pure absorption cases, while the solid lines trace cases including scattering. The 2σ level uncertainties are shown as shaded regions. The emission is at least marginally optically thick for the more general cases (with scattering), with the peak values of τ_ν decreasing to ~ 0.01 for the longest wavelength if scattering is excluded. The resulting grain size and dust surface density profiles, on the other hand, are shown in Figure 6. The white solid line highlights the most probable profiles in both cases. The dust ring seems to be composed of particles with a maximum grain size of ~ 0.61 mm. We remark that, similar to the case of the spectral index of Figure 4, the $a_{\max}$ estimate is only reliable from 60 to 120 au, where the emission from the dusty disk is expected.

A similar analysis, but using a slope for the particle size distributions of $q = 2.5$ and $q = 3.5$, is shown in Appendix A. Overall, we did not find a significant change in $a_{\max}$, which has average values of 0.56 mm and 0.65 mm for $q = 2.5$ and $q = 3.5$, respectively. It is worth noting that ignoring scattering effects and assuming the disk to be optically thin could easily lead to the overestimation of dust particle sizes in protoplanetary disks, as
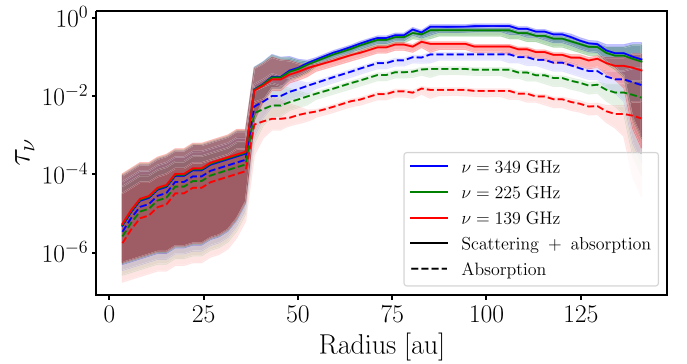

Figure 5. The optical depth profiles for the ALMA band 4 (red), band 6 (green), and band 7 (blue) observations. The dashed lines indicate pure absorption cases, while the solid lines show optical depths for cases also including scattering. The 2σ level uncertainties are shown as shaded regions.

shown by our more realistic estimates of $a_{\max}$, which are between ~ 2 and up to 4 times smaller than the $a_{\max}$ obtained through the classical approach in Section 3.3.1.

3.4. Dust Mass

Using the dust surface density obtained from our multiwavelength analysis, as described in Section 3.3.2, we can estimate the total dust mass in the disk around Sz 91 by integrating the Σ_d profile of Figure 6 over the disk area. By doing so, we found a total dust mass of $M_{\mathrm{dust}} = 31.3^{+6.3}_{-10.6}\ M_\oplus$ (also shown in the left panel of Figure 6 in solar masses). Our dust mass estimate is 3.4 times larger than the value found in Canovas et al. (2015), of $M_{\mathrm{dust}} = 9.08\ M_\oplus$ (scaled to the same distance), estimated from fitting the entire SED (from the optical to the millimeter) with the assumption that $a_{\max} = 1$ mm. On the other hand, our M_{dust} is ~ 2 times higher than the dust mass estimated in van der Marel et al. (2018), with a value of $M_{\mathrm{dust}} = 15.8\ M_\oplus$ (also scaled to the true distance).

In order to compare the dust masses obtained from submillimeter surveys, where the dust emission is usually assumed to be optically thin, we also estimated M_{dust} using the simplified relationship of Hildebrand (1983), which correlates the dust mass and the millimeter continuum flux as:

$$M_{\mathrm{dust}} = \frac{F_\nu d^2}{\kappa_\nu B_\nu(T_d)} \simeq 3.707 \left(\frac{F_{2\mathrm{mm}}}{\mathrm{mJy}}\right)\left(\frac{d}{150\ \mathrm{pc}}\right)^2 M_\oplus, \qquad (6)$$

where F_ν is the mm flux at 2.1 mm; d is the source distance from Gaia EDR3; T_d is the assumed dust temperature; B_ν is the Planck function at T_d; and κ_ν is the dust grain opacity. To be able to make comparisons with other measurements in the literature, we followed the assumptions used by Ansdell et al. (2016, 2018) and Tazzari et al. (2021) in the Lupus surveys at 0.9, 1.3, and 3.0 mm, respectively. We adopted a power-law opacity of the form $\kappa_\nu = 10\ (\nu/1000\ \mathrm{GHz})^\beta$ cm^2 g^{-1}, with a β value of 1 (Beckwith et al. 1990), which yields $\kappa_{2.1\mathrm{mm}} = 1.46$ cm^2 g^{-1}, assuming isothermal dust with a temperature $T_d = 20$ K, the median for Taurus disks (Andrews & Williams 2005). Using Equation (6), we found a dust mass of $M_{\mathrm{dust}} = 8.89\ M_\oplus$. This is consistent with other works in the literature stating that disk masses can often be underestimated by a large fraction by assuming an optically thin emission (e.g., Galván-Madrid et al. 2018).

This highlights the impact of assuming an optically thin emission and not including scattering effects when estimating
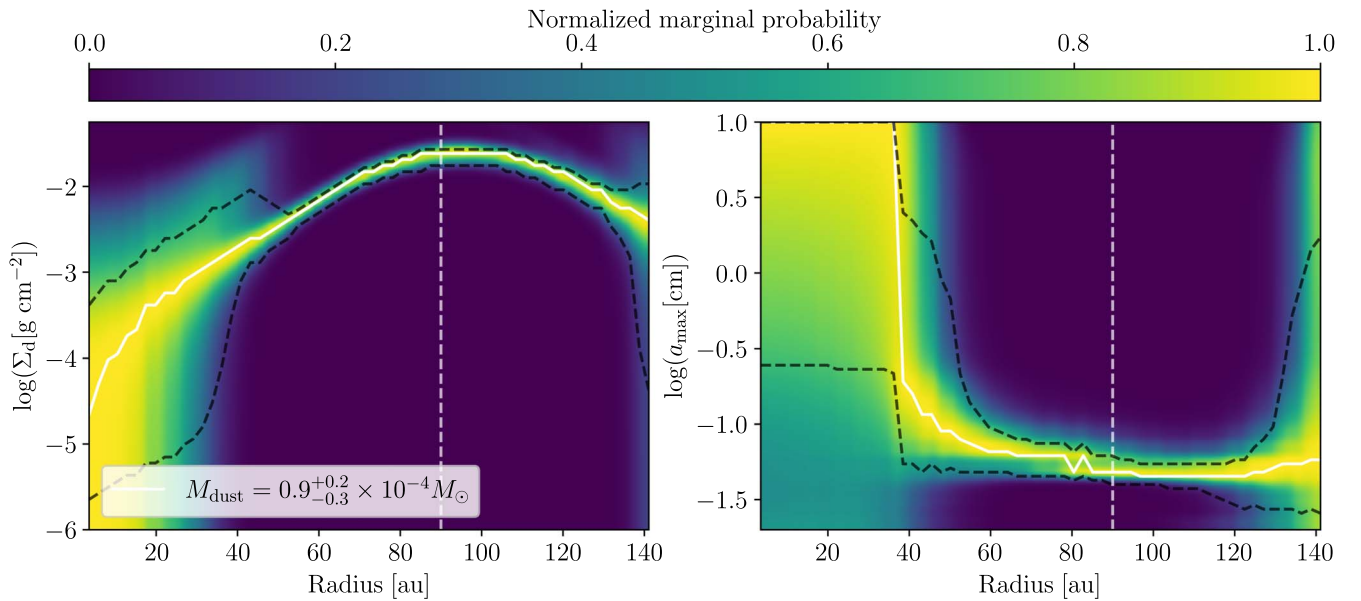
Figure 6. The radial fitting of the millimeter spectrum (see Section 3.3 for details). Probability distributions of the surface density (left) and maximum grain size (right) are shown as a function of radius, where the color bar shows the marginal probability. The white solid lines indicate the best fit. The black dashed lines represent the 2σ level uncertainties. The vertical lines indicate the location where the dust emission peaks (90 au). The total dust mass in the ring is 31.3 $M_{\oplus}$ and the maximum grain size is $\sim$0.61 mm.

dust masses. Even though our optical depths were less than 1 in all the data sets, it seems that having only marginally optically thick regions may lead to the underestimation of the dust mass when using Equation (6). Overall, it seems that the main factor contributing to the underestimation of dust masses in (sub) millimeter surveys is the disregarding of optical depth and scattering effects. This may be a solution to the mass budget problem for planet formation—the masses of the solids in (sub) millimeter surveys of protoplanetary disks seems to be too low to explain the observed exoplanetary systems.

4. Discussion

The transition disk around the low-mass star Sz 91 has a structure composed of millimeter-sized particles located in a well-defined ring, a large dust-depleted cavity, and smaller dust particles inside this millimeter cavity (as shown by polarimetric observations). Therefore, Sz 91 represents a clear example of dust filtering and radially confined dust particles. We have presented new ALMA band 4 observations of the dust ring and, by combining the new data with previous ALMA observations in band 7 and band 6, we have derived the spectral index, optical depth, and maximum grain size in the ring. We have found the spectral indices, as well as the maximum particle size, to be nearly constant in the ring, and the emission to be only marginally optically thick. In what follows, we discuss the implications of these findings for the evolutionary status of the disk, and compare Sz 91 with the disk population in Lupus, as well as with transition disks in other regions.

4.1. Grain Growth and Possible Planetesimal Formation in the Ring Around Sz 91

Our results imply that the dust particles in the Sz 91 disk have grown to at least 0.61 mm in size. Given the ringlike structure of this source, it is now clear that dust is accumulating in a dust trap produced by the local pressure maxima sculpting the ring. ALMA observations are only sensitive to submillimeter particles,

so centimeter particles may also be present in the disk. Therefore, understanding the disk around Sz 91 requires the modeling of particle growth, including fragmentation, and eventually planetesimal formation by the streaming instability, which has recently been reported to be a robust process in pressure bumps (Guilera et al. 2020; Carrera et al. 2021).

In this line of reasoning, Stammler et al. (2019) have explained the nearly constant optical depth of substructures in the DSHARP targets, by including dust growth and fragmentation, as well as planetesimal formation through the streaming instability, in a one-dimensional simulation of dust evolution designed especially for the second dust ring of the protoplanetary disk around HD 163296. Even though HD 163296 has a stellar luminosity of 17 $L_{\odot}$, significantly higher than that of Sz 91, these simulations are particularly helpful for interpreting our observational results, as the ring in the model is located at a similar distance from the central star and is of a similar width as the millimeter ring around Sz 91. Moreover, since the model used in Stammler et al. (2019) is composed of a disk with a gap at 83.5 au, the influence of stellar irradiation will be more significant in the inner regions and should not affect the evolution of the second dust ring directly.

The model in Stammler et al. (2019) is largely based on that in Birnstiel et al. (2010), but includes planetesimal formation when a dust-to-gas mass ratio of unity is reached in the disk midplane. While the equilibrium reached between grain growth and fragmentation is not affected by the inclusion of planetesimal formation, the optical depth is kept at values similar to those derived from observations of the DSHARP rings. The obtained peak optical depth in the simulations first increases with time, until planetesimal formation due to the streaming instability removes the millimeter particles from the midplane, which leads to a decrease in optical depth. For ages ranging from 0.1 to 13 Myr, the peak optical depth varies between 0.2 and 0.6 (see their Figure 2). The spectral index in the ring reaches nearly constant values of $3.0 - 3.5$ for ages between 1 and 13 Myr (their Figure 5).

Sz 91 is between 3 and 5 Myr old (Maucó et al. 2020), and the spectral index inside the ring is nearly constant, with values ranging from 3.3 to 3.5. The peak optical depth we measured from our observations covered the range of 0.2 to 0.6 for the three observed bands, when scattering was included, and it ranged between 0.01 and 0.1 for the pure absorption case. The ring around Sz 91 can therefore be added to the DSHARP sample of rings clustering in a close range of optical depth. In addition, both the spectral index as well as the optical depth perfectly match the predictions of the model presented in Stammler et al. (2019). It therefore appears plausible that planetesimal formation is ongoing in the ring around Sz 91. While the agreement between the predictions and the observations seems robust, we advocate some caution, as the model presented in Stammler et al. (2019) does not include scattering effects in the determination of the optical depth, which is inconsistent with the values derived from observations indicating that scattering plays a role (if the emission is not optically thin). Also, as noted by Stammler et al. (2019), their model does not include the backreaction of dust particles onto the gas, which can smear out concentrations (Taki et al. 2016; Gárate et al. 2019).

Alternatively, Zhu et al. (2019) have shown that optically thick scattering disks can also explain the peak optical depths observed in the DSHARP sample. They explained how the optically thin assumption may be incorrectly applied to an optically thick disk with reduced emission due to scattering. However, this scenario only applies to the inner disk within 50 au. Since our source consists of a dusty ring beyond 60 au, where the emission can be well fitted with a Gaussian profile along the radial direction, the scenario proposed by Zhu et al. (2019) might not be applicable in our case. Furthermore, when the disk is large, most of the dust mass is in the outer disk, which is generally optically thin at 2.1 mm. If this is the case, then the disk mass obtained with Equation (6), assuming optically thin emission, should underestimate the mass only by a factor of $\sim$2 (Zhu et al. 2019) in comparison to the mass obtained from our detailed analysis of the millimeter spectrum including scattering. This is similar to what we have found in this work (within the uncertainties), considering that the emission is actually marginally optically thick.

Additionally, the high value of the spectral index ($\alpha \sim 3.34$) in the ring around Sz 91 is also in line with the emission not being optically thick. Therefore, we can conclude that the dust emission at band 4 as shown here can be used to properly characterize the dust particles in the ring, which, according to our observational results, comprise dust particles with a maximum grain size of at least 0.61 mm. Given the observed optical depth and the spectral index in the ring, ongoing planetesimal formation is a likely scenario for explaining these observational signatures.

4.2. Comparison with Disks in Lupus

Thanks to the advent of ALMA, large surveys of disk populations have been conducted at millimeter wavelengths. Several authors have now focused their attention on tackling disk evolution through disk demographics. Two particular works have been conducted in the Lupus star-forming region, aiming to characterize grain growth (Tazzari et al. 2021; Ansdell et al. 2016, 2018). Tazzari et al. (2021) found spectral indices for the 35 brightest Class II disks of $\alpha_{1-3\,mm} < 3$ with a mean value of 2.23 (see Figure 7). Note that Sz 91 was not
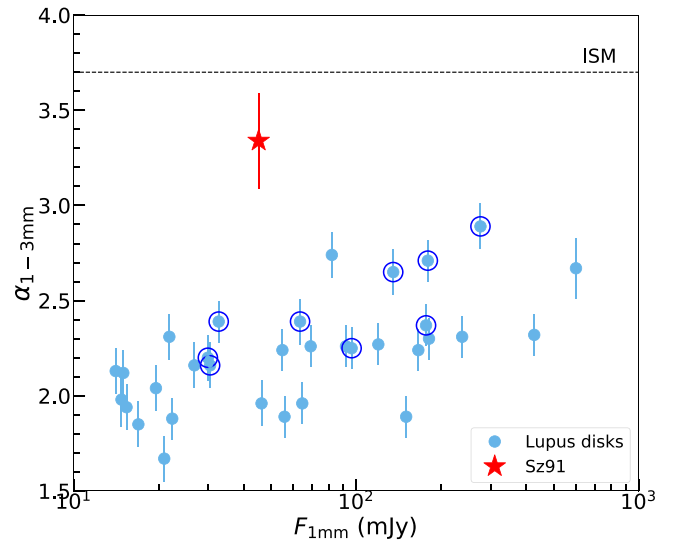

Figure 7. The spectral index between 1 and 3 mm as a function of integrated 1 mm flux for Lupus disks (blue filled circles) from Tazzari et al. (2021). Transition disks are marked with an additional blue circle. The 1 mm flux is taken from Ansdell et al. (2018). The dashed line is the typical $\alpha_{1-3\,mm}$ of the optically thin emission of ISM dust. The red star indicates the position of Sz 91 using our estimate of α from 1 to 2.1 mm. Sz 91 appears as an outlier, with the highest α value of 3.34 among the Lupus disk population.

observed in this work, due to an erroneous observational setup. They found a tendency of larger values for transition disks ($\alpha_{TD} \sim 2.5$, marked by an additional blue circle in Figure 7), something also found at shorter wavelengths by Ansdell et al. (2018), using fluxes from 0.9 to 1.33 mm. They interpreted this as evidence of grain growth (in the optically thin and Rayleigh–Jeans regimes), with the maximum grain sizes being larger than 1 mm for a range of reasonable dust composition and porosity levels.

In the context of the Lupus disk population, Sz 91 stands as the source with the highest spectral index. In Figure 7, we compare the $\alpha_{1-3\,mm}$ reported in Tazzari et al. (2021) with that for Sz 91 estimated here ($\alpha_{1-2.1mm}$, red star) as a function of their 1 mm fluxes. The spectral index of 3.34 plotted in the figure and found in Section 3.2 is totally consistent with the disk integrated spectral index estimated from the fluxes reported in Section 2. At 220 mas resolution, for instance, we obtained $\alpha_{1-2.1mm} = 3.31 \pm 0.26$. Consistent with previous findings that transition disks seem to have larger spectral indices than full disks, the spectral index of Sz 91 is $\sim$1.5 times larger than the other disks in Lupus, and similar to the other transition disks in Lupus (identified in van der Marel et al. 2018).

Ansdell et al. (2018) mentioned that one of the reasons for the low α, especially for brighter disks, may be attributed to larger optically thick regions in the more massive disks, something also mentioned in Galván-Madrid et al. (2018). In this regard, we estimated the optical depths for the three data sets used in this work. Figure 5 shows that the emission in all three ALMA bands is optically thin if we only consider absorption (dashed lines), and it is still lower than 1 in the more general case including scattering (solid lines). Given the large cavity around this source ($R_{cav} \sim 86$ au; Francis & van der Marel 2020), where lower temperatures are expected for dust at such large radii, it is not surprising that the dust emission is optically thin at millimeter wavelengths. The absence of
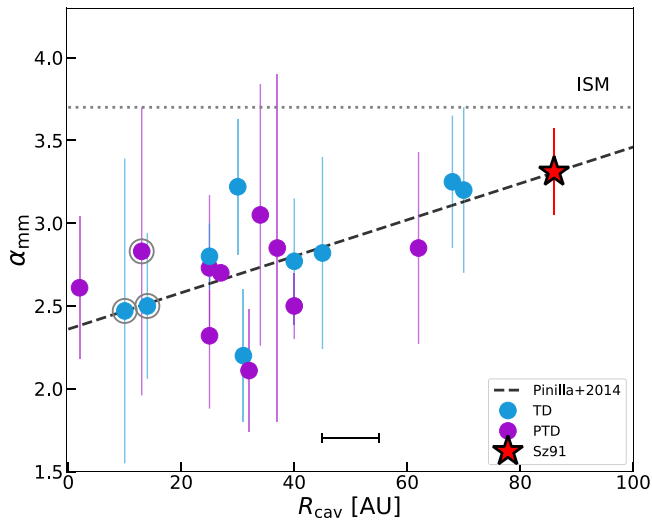
Figure 8. The integrated spectral index between ∼1 and ∼3 mm as a function of the cavity radius for the sample of transition disks in Pinilla et al. (2014). Sz 91 has also been plotted for the purpose of comparison (red star). The dashed line shows the α_{mm}–R_{cav} relationship found in Pinilla et al. (2014). Objects with detected inner disks (pretransition disks) are indicated as purple dots. The error bar at the bottom indicates the average error in the cavity radius. Sources with cavity sizes estimated through SED-fitting are indicated with an additional gray circle.

optically thick regions in the disk around Sz 91 may be the reason for its particularly high spectral index.

Furthermore, as pointed by Zhu et al. (2019), if observations have measured α as $\lesssim 2$, this could be a strong indication that the disk is optically thick at those wavelengths and that dust scattering plays an important role. They explained that values as low as 2 for the spectral index are not likely to occur in optically thin disks. If the disk is optically thick at the inner disk and optically thin at the outer disk, for instance, then the spectral index will be around 2 at the inner disk (which is optically thick) and then suddenly change to 3–4 when $\tau < 1$. This is simply because α is determined by different physical mechanisms in the optically thick and thin regimes. Therefore, the increase of α at the outer disk observed in some systems may be due to the whole disk becoming optically thin. In fact, this scenario is particularly suitable to the Lupus region, since most of its disk population is composed of compact (small) disks (Ansdell et al. 2018; Tazzari et al. 2021), which are most likely optically thick at ALMA bands, and hence will have lower spectral indices than those of more extended disks, as is the case for Sz 91.

4.3. Comparison with Transition Disks in Other Regions

To inquire if Sz 91 also stands out when compared to other transition disks in different star-forming regions, we have plotted in Figure 8 the integrated spectral index from ∼1 to ∼3 mm, α_{mm}, as a function of cavity size, for the sample of transition disks reported in Pinilla et al. (2014). The values of α_{mm} were taken from their tables 1 and 2, except for SR 24S and SR21, which were taken from the more recent works of Pinilla et al. (2019) and Pinilla et al. (2015b), respectively.

The sizes of the cavities for each source, R_{cav}, were taken from Pinilla et al. (2014), except for those objects with updated sizes, for which we have used the most recent values: CS Cha, DM Tau, DoAr 44, GM Aur, MWC 758, T Cha, TWHya, UX Tau A, and WSB 60 from Francis & van der Marel (2020); J1604-2130, LkCa15, and SR 21 from van der Marel et al.

(2015); SR 24 S from Cieza et al. (2021); and SZ Cha from Ribas et al. (2016). Sources with cavity sizes estimated through SED-fitting are indicated by an additional gray circle. The error bar at the bottom shows the average error expected for the cavity size (±5 au). Finally, objects with detected inner disks in the Francis & van der Marel (2020) survey have been identified as pretransition disks (PTD) in the figure.

Pinilla et al. (2014) found a correlation between the disk integrated spectral index and the cavity size in (pre)transition disks (the dashed line in Figure 8). They explained that it was because the millimeter emission is dominated by the dust at R_{cav} (i.e., in the pressure bump). Therefore, disks with wider cavities (pressure bumps located further out from the star) will have a smaller a_{max}. The smaller grains will then experience a lower radial drift, making turbulent motions the main source of destructive collisions. In this case, the a_{max} is reached when the fragmentation velocity of the particles equals the turbulent relative velocity. At this point, a_{max} will also scale with the gas surface density of the disk, which decreases with the distance to the star.

Sz 91 perfectly fits the α_{mm}–R_{cav} relationship of Pinilla et al. (2014), which is consistent with our estimate of $a_{\mathrm{max}} = 0.61$ mm, i.e., in the submillimeter range (see Section 3.3.2). In this regard, Sz 91 follows the expected behavior of a transition disk with a large cavity. Since it hosts the largest cavity around a single T Tauri star (and the largest one in the sample plotted on the figure), it is expected to possess the highest spectral index, which is, indeed, the case. This reinforces our findings in Figure 7, where the significant difference between the spectral index of Sz 91 and the disk population in Lupus was due to the latter being mostly composed of compact (small) disks.

5. Conclusions

In this paper, we have presented new ALMA band 4 (2.1 mm) observations of the transition disk Sz 91, combined with archival band 6 (1.3 mm) and band 7 (0.9 mm) data. The main results can be summarized as follows:
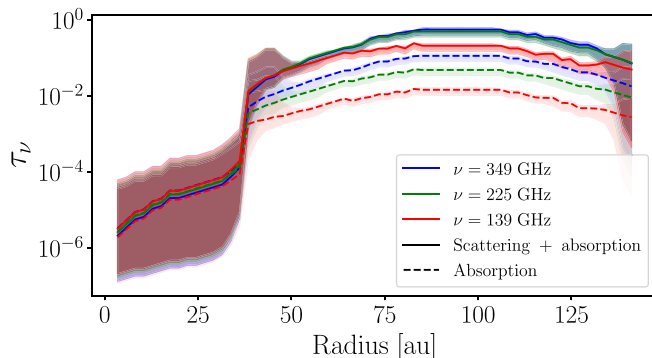
1. We obtained 2.1 mm ALMA observations at ∼0″1 resolution and a sensitivity of 5.4 μJy beam^{-1}. The continuum image shows a well-resolved ring of dust peaking at ∼90 au from the central star.

2. By combining the new 2.1 mm observations with the previous ALMA observations at 0.9 and 1.3 mm at 220 mas resolution, we derived the spectral index of the disk around Sz 91, and found it to be constant throughout the ring, with $\alpha \sim 3.34 \pm 0.26$ and not showing clear azimuthal variations. By comparing this value with the spectral indices reported in the literature for the disk population in Lupus, we found that Sz 91 exhibits the highest α of the region. Optically thick regions in the disks around nonresolved Lupus sources may account for the lower α values.

3. We estimated the maximum grain sizes in the ring around Sz 91 by applying two different approaches. First, by assuming an optically thin emission, and without including scattering effects, we found a slope of the absorption coefficient of $\beta_{\mathrm{abs}} = 1.34$, which requires grains with 1.0 mm $< a_{\mathrm{max}} < 2.5$ mm. Second, in a more realistic approach including scattering effects, and by performing a radial analysis of the millimeter spectrum without putting any constraints on the optical depth at any wavelength (following Carrasco-González et al. 2019), we found that the dust ring was composed of particles with a maximum

grain size of $a_{max} \sim 0.61$ mm. Scattering effects must be taken into account when characterizing the dust content in protoplanetary disks if one wishes to avoid overestimating the maximum grain size.

4. Sz 91 perfectly fits the relationship found in Pinilla et al. (2014) between integrated spectral index and cavity size for transition disks. Given its large cavity (~ 86 au), it has the highest spectral index of the transition disk sample considered here. This is consistent with our a_{max} estimate lying in the submillimeter range, and it reinforces the fact that the significant difference between the spectral index of Sz 91 and the Lupus population is due to the latter being mostly composed of small disks.

5. The disk emission is marginally optically thick for the more general case (with scattering), with a peak optical depth between 0.2 and 0.6, decreasing to $\tau_\nu \sim 0.01$ for the longest wavelength (if scattering is excluded). These values for the disk around Sz 91 are in the same range as those for the DSHARP targets.

6. The total mass of the solids that we obtained by integrating the expected surface density profile from our multi-wavelength analysis, considering the effects of optical depth and self-scattering, was $M_{dust} = 31.3^{+6.3}_{-10.6}$ $M_\oplus$. Lower dust masses, by at least a factor of 2, are found if one assumes the emission to be optically thin.

We interpret these findings as evidence of ongoing grain growth produced by the trapping of dust in a pressure bump. The nearly constant spectral index and range of optical depth values found in the ring around Sz 91 agree very well with the predictions of planetesimal formation of Stammler et al. (2019). Given the self-regulating nature of this process (which stabilizes the dust-to-gas mass ratio in the midplane), along with the steady state between particle growth and fragmentation, after 1 Myr the spectral index of the ring has reached its minimum value, and enough millimeter particles have been converted to planetesimals as to constrain the optical depths to the observed values. Sz 91, therefore, represents a plausible case of possible planetesimal formation in a transition disk. Future multi-wavelength observations resolving the disk ring radially could provide crucial additional constraints on models of planetesimal and planet formation.

Appendix A
SED-fitting Using Different Power-law Indices for the Particle Size Distributions

The optical depth profiles obtained for the ring around Sz 91 using a power-law index for the particle size distribution of $q = 2.5$ are shown in Figure 9 (left panel). The red, green, and blue lines indicate the ALMA band 4, 6, and 7 optical depths, and the dashed lines represent the pure absorption case, while the solid lines trace cases that also consider scattering. The
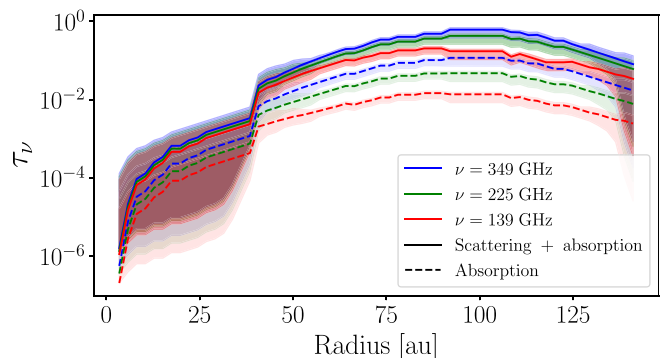

Figure 9. Optical depth profiles for ALMA band 4 (red), band 6 (green), and band 7 (blue) observations, estimated using a slope for the particle size distributions of $q = 2.5$ (left) and $q = 3.5$ (right). The dashed lines indicate pure absorption cases, while the solid lines show optical depths for cases that also include scattering. The 2σ level uncertainties are shown as shaded regions.
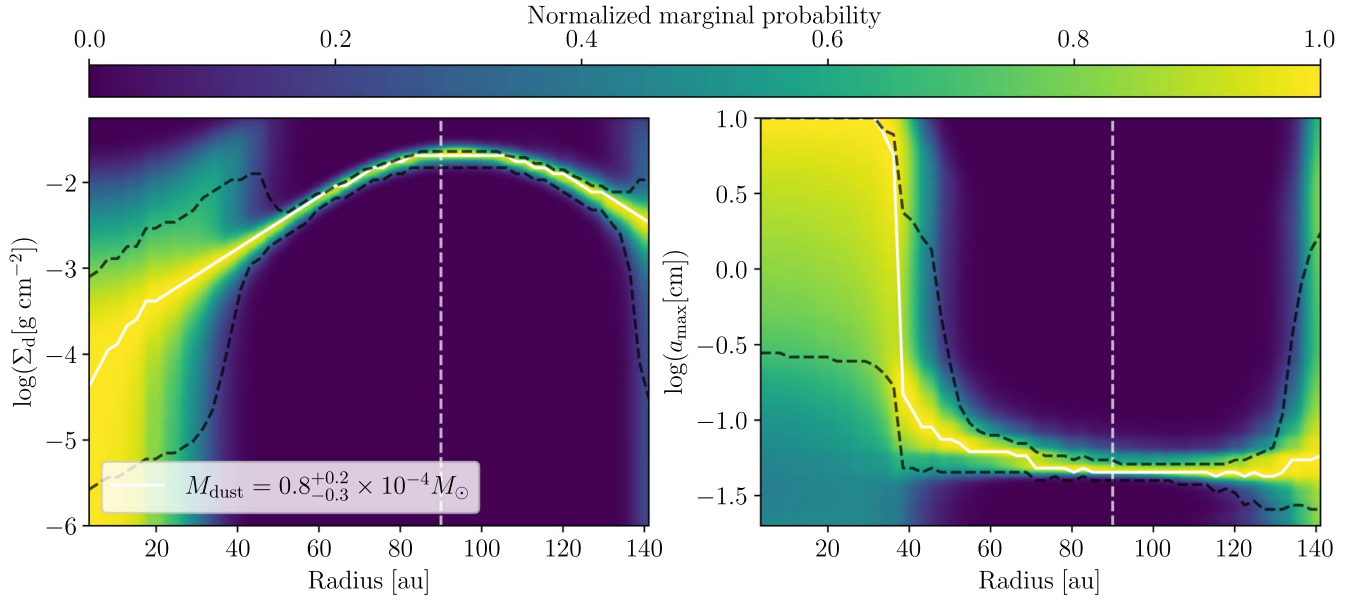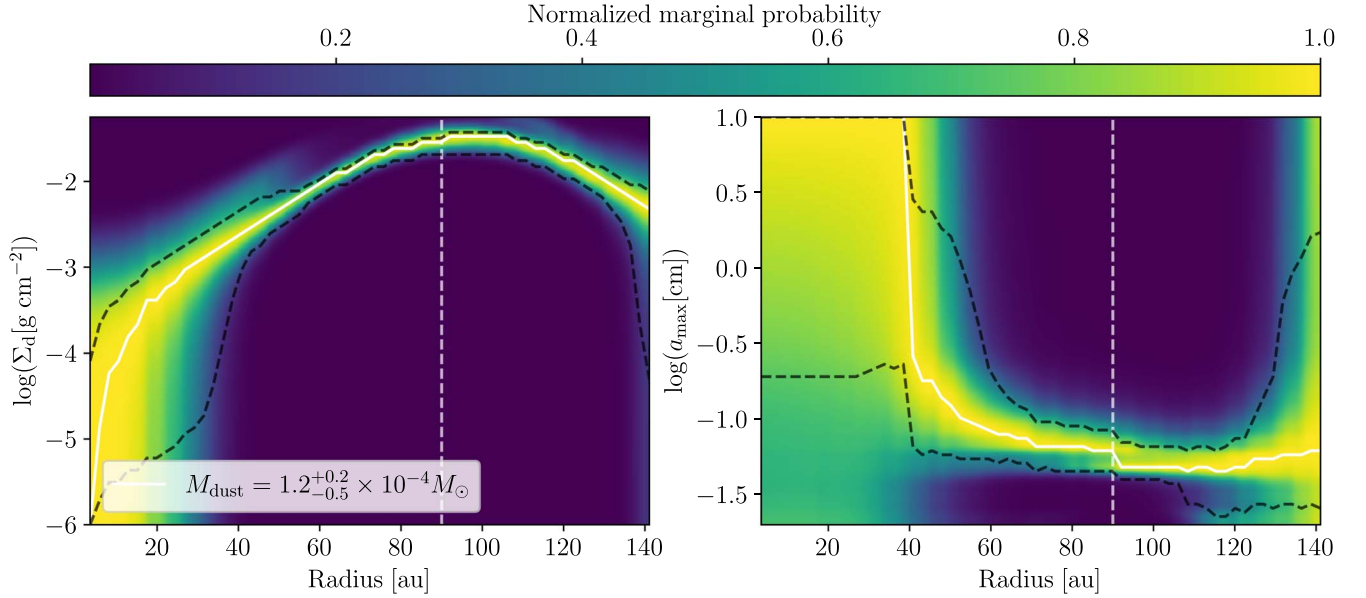
Figure 10. The radial fitting of the millimeter spectrum (see Section 3.3 for details), using a power-law index for the particle size distribution of $q = 2.5$. Probability distributions of the surface density (left) and maximum grain size (right) are shown as a function of radius, where the color bar shows the marginal probability. The white solid lines indicate the best fit. The black dashed lines represent the 2σ level uncertainties. The vertical lines indicate the location where the dust emission peaks (90 au). The total dust mass in the ring is $27^{+7}_{-10}\,M_\oplus$ and the maximum grain size is $\sim$0.56 mm.

Figure 11. The radial fitting of the millimeter spectrum (see Section 3.3 for details), using a power-law index for the particle size distribution of $q = 3.5$. Probability distributions of the surface density (left) and maximum grain size (right) are shown as a function of radius, where the color bar shows the marginal probability. The white solid lines indicate the best fit. The black dashed lines represent the 2σ level uncertainties. The vertical lines indicate the location where the dust emission peaks (90 au). The total dust mass in the ring is $40^{+7}_{-17}\,M_\oplus$ and the maximum grain size is $\sim$0.65 mm.

resulting grain sizes and dust surface densities, on the other hand, are shown in Figure 10. We found an $a_{max} = 0.56$ mm and an $M_{dust} = 27^{+7}_{-10}\,M_\oplus$.

These results are similar to the canonical value of $q = 3.5$, as shown in Figure 9 (right panel) and Figure 11, where the symbols and colors are the same as those in Figure 10. The main difference is that the maximum grain size is less constrained in the canonical case, with an average value of 0.65 mm, and the dust mass is $40^{+7}_{-17}\,M_\oplus$, 1.5 times higher than for the case of $q = 2.5$.

Appendix B
Line Imaging

Even though the main focus of this work has been based on continuum observations, we centered one of our four spectral windows at the rest frequency of the carbon monosulfide (CS v = 0, 3–2) line at 146.96 GHz, aiming for a possible detection.

As shown in Figure 12, we detected the CS(3–2) line at velocities ranging from $\sim$3 to $\sim$5 km s^{-1}. The rms of the CLEAN image was 0.33 mJy beam^{-1}. The emission peaked at $\sim$3 km s^{-1}, with an intensity peak of 2.11 mJy beam^{-1} (6.5σ).
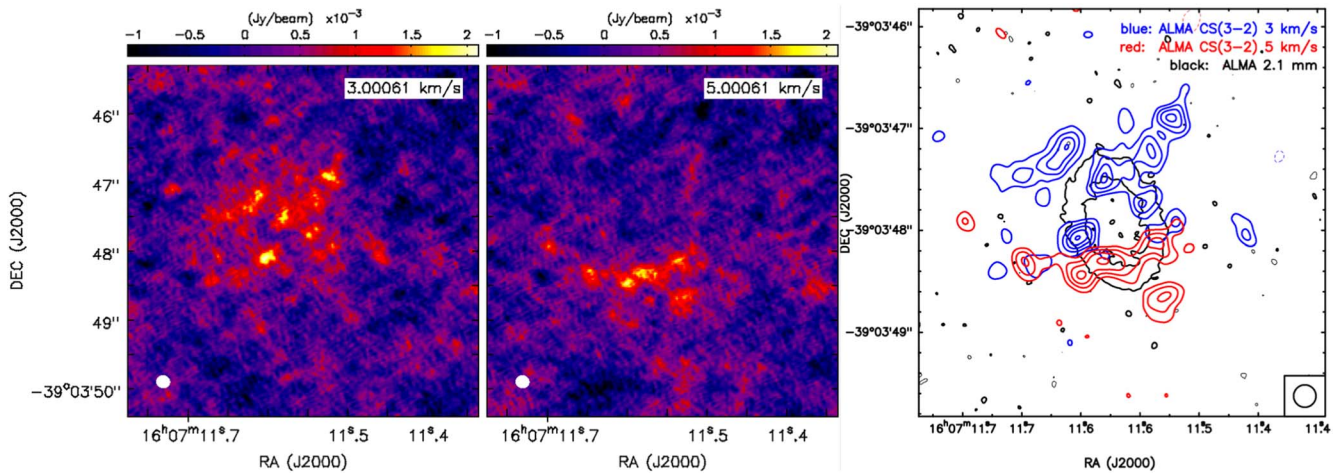
Figure 12. *Left:* the CS v = 0, (3–2) line continuum-subtracted CLEAN image. We detect the line at the velocity range from ∼3 to ∼5 km s^{-1}. The emission peaks at 3 km s^{-1}, with an intensity peak of 2.11 mJy beam^{-1} (6.5σ). The beam size of 197 × 180 mas is shown as a filled circle at the bottom left of each panel. *Right:* the CS v = 0, (3–2) emission of the blue and red channels of the cube, after smoothing to a final beam of 0″.22 (shown at the bottom right). The blue and red contours correspond to 3, 4, 5, 6, and 7 times the rms of the smoothed cube (∼0.33 mJy/beam). The black contours correspond to the 3σ contour of the 2.1 mm continuum image.
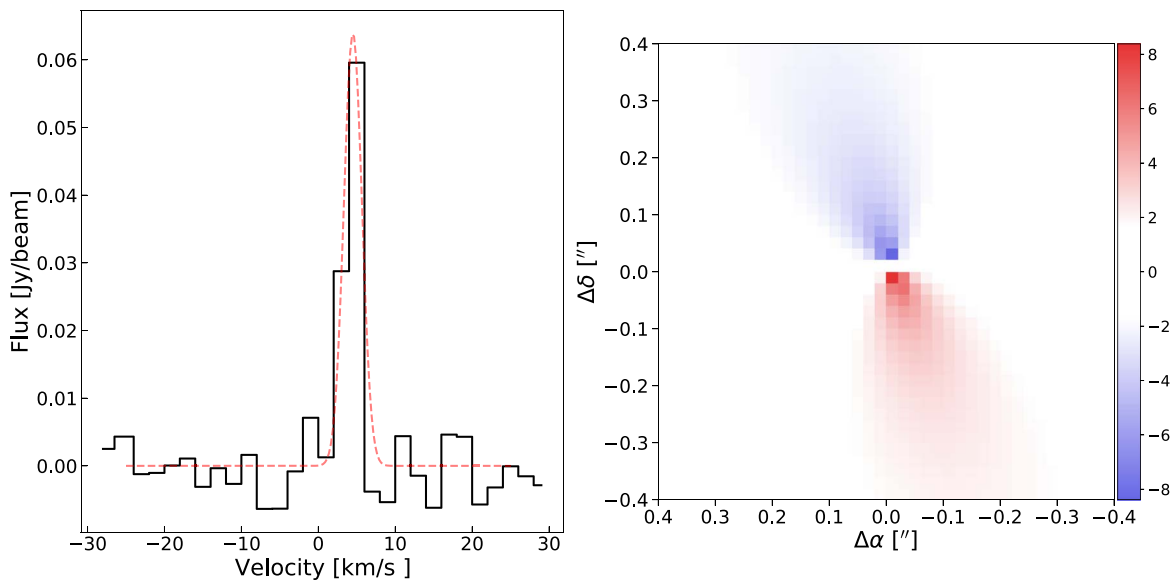
Figure 13. The CS Line Spatial Filtering results. *Left:* the shifted spectrum. The line is clearly detected at 4.5 ± 0.1 km s^{-1}, given by the Gaussian fit (the red dashed line). *Right:* the disk model. The color coding corresponds to the estimated Keplerian velocity for each pixel.

The right panel shows the CS(3–2) emission of the blue and red channels of the cube, after smoothing to a final beam of 0″.22 (shown at the bottom right). The blue and red contours correspond to 3, 4, 5, 6, and 7 times the rms of the smoothed cube (∼0.33 mJy/beam). It is worth noting that there are at least five peaks of CS emission that match the dusty ring very well in spatial terms. Of these five peaks of gas emission, two peaks were detected at 5σ, two peaks were detected at 6σ, and one peak was detected at 7σ. Therefore, we have certainly detected CS(3–2) gas associated with the dusty ring. In addition, there were other peaks further away that could be related to accretion streams or simply be part of the Keplerian pattern that has already been shown by Tsukagoshi et al. (2019) at CO(3–2) and HCO$^+$(4–3).

In order to boost the signal of the CS line (3–2) at 146.96 GHz, we used the spectral and spatial filtering technique (Matrà et al. 2017). The idea is to "correct" the velocity of each pixel in the data cube to account for the Keplerian rotation of

the disk. To this end, for each pixel, we computed the Keplerian velocity, accounting for the inclination and position angles of the disk obtained from the ALMA band 7 (0.9 mm) observations of Tsukagoshi et al. (2019). We assumed a stellar mass of 0.58 $M_\odot$ (Maucó et al. 2020), and we tested for both direction of rotation. Then for each pixel of the data cube, we shifted the one-dimensional spectrum by the opposite of the estimated velocity. Afterwards, for each velocity frame, we summed the total flux in a circular aperture of 1″.5 size. If a line was present in the observations, its signal would have been significantly increased, as it should have been shifted into a single (ideally) velocity frame. The two main caveats to this approach are that we assumed the disk to be vertically flat, and that the gas was rotating at Keplerian velocity (since it may be rotating at subKeplerian velocity if it is self-supported by its own pressure). Figure 13 shows the results of the analysis. The left panel shows the shifted spectrum, and a line is clearly detected at 4.5 ± 0.1 km s^{-1}, as shown by the Gaussian fit (the

red dashed line). This value is consistent with the radial velocity of the star reported in Canovas et al. (2015), 3.4 ± 0.2 km s^{-1}, within a factor of less than one. The right panel shows the disk model, where the color coding corresponds to the estimated Keplerian velocity for each pixel.

The CS line traces dense gas, and it is now commonly observed in protoplanetary disks (Guilloteau et al. 2016; Dutrey et al. 2017; Teague et al. 2018; Phuong et al. 2018; Fuente et al. 2010; Le Gal et al. 2019). However, it is mostly observed in one of the higher transitions (5–4, 6–5). We report here the less common lower (3–2) transition that could be used in combination with future detections of CS at higher transitions in order to estimate the excitation temperature of the gas emitting the line.

ORCID iDs

Karina Maucó ⓘ https://orcid.org/0000-0001-8284-4343
Carlos Carrasco-González ⓘ https://orcid.org/0000-0003-2862-5363
Matthias R. Schreiber ⓘ https://orcid.org/0000-0003-3903-8009
Anibal Sierra ⓘ https://orcid.org/0000-0002-5991-8073
Johan Olofsson ⓘ https://orcid.org/0000-0003-4475-3605
Amelia Bayo ⓘ https://orcid.org/0000-0001-7868-7031
Claudio Caceres ⓘ https://orcid.org/0000-0002-6617-3823
Hector Canovas ⓘ https://orcid.org/0000-0001-7668-8022
Aina Palau ⓘ https://orcid.org/0000-0002-9569-9234

References

Alcalá, J. M., Manara, C. F., Natta, A., et al. 2017, A&A, 600, A20
Alexander, R. D., & Armitage, P. J. 2007, MNRAS, 375, 500
Partnership, A. L. M. A., Brogan, C. L., Pérez, L. M., et al. 2015, ApJL, 808, L3
Andrews, S. M., & Williams, J. P. 2005, ApJ, 631, 1134
Andrews, S. M., Wilner, D. J., Espaillat, C., et al. 2011, ApJ, 732, 42
Andrews, S. M., Huang, J., Pérez, L. M., et al. 2018, ApJ, 869, L41
Ansdell, M., Williams, J. P., van der Marel, N., et al. 2016, ApJ, 828, 46
Ansdell, M., Williams, J. P., Trapman, L., et al. 2018, ApJ, 859, 21
Astropy Collaboration, Robitaille, T. P., Tollerud, E., et al. 2013, A&A, 558, A33
Barenfeld, S. A., Carpenter, J. M., Sargent, A. I., Isella, A., & Ricci, L. 2017, ApJ, 851, 85
Barrett, P., Hunter, J., Miller, J. T., Hsu, J.-C., & Greenfield, P. 2005, in ASP Conf. Ser., 347, Astronomical Data Analysis Software and Systems XIV, ed. P. Shopbell, M. Britton, & R. Ebert (San Francisco, CA: ASP), 91
Beckwith, S. V. W., & Sargent, A. I. 1991, ApJ, 381, 250
Beckwith, S. V. W., Sargent, A. I., Chini, R. S., & Guesten, R. 1990, AJ, 99, 924
Birnstiel, T., Ricci, L., Trotta, F., et al. 2010, A&A, 516, L14
Birnstiel, T., Dullemond, C. P., Zhu, Z., et al. 2018, ApJ, 869, L45
Calvet, N., D'Alessio, P., Hartmann, L., et al. 2002, ApJ, 568, 1008
Canovas, H., Caceres, C., Schreiber, M. R., et al. 2016, MNRAS, 458, L29
Canovas, H., Schreiber, M. R., Cáceres, C., et al. 2015, ApJ, 805, 21
Carrasco-González, C., Sierra, A., Flock, M., et al. 2019, ApJ, 883, 71
Carrera, D., Simon, J. B., Li, R., Kretke, K. A., & Klahr, H. 2021, AJ, 161, 96
Casassus, S., van der Plas, G. M., Perez, S., et al. 2013, Natur, 493, 191
Christiaens, V., Casassus, S., Perez, S., van der Plas, G., & Ménard, F. 2014, ApJL, 785, L12
Cieza, L. A., González-Ruilova, C., Hales, A. S., et al. 2021, MNRAS, 501, 2934
Dong, R., Li, S., Chiang, E., & Li, H. 2017, ApJ, 843, 127
Drążkowska, J., Li, S., Birnstiel, T., Stammler, S. M., & Li, H. 2019, ApJ, 885, 91
Dullemond, C. P., Birnstiel, T., Huang, J., et al. 2018, ApJ, 869, L46
Dutrey, A., Guilloteau, S., Piétu, V., et al. 2017, A&A, 607, A130
Flock, M., Ruge, J. P., Dzyurkevich, N., et al. 2015, A&A, 574, A68
Francis, L., & van der Marel, N. 2020, ApJ, 892, 111
Fuente, A., Cernicharo, J., Agúndez, M., et al. 2010, A&A, 524, A19
Gaia Collaboration, Brown, A. G. A., Vallenari, A., et al. 2012, arXiv:2012.01533
Gaia Collaboration, Prusti, T., de Bruijne, J. H. J., et al. 2016, A&A, 595, A1
Galván-Madrid, R., Liu, H. B., Izquierdo, A. F., et al. 2018, ApJ, 868, 39
Gárate, M., Birnstiel, T., Drazkowska, J., & Stammler, S. M. 2019, AAS/Division for Extreme Solar Systems Abstracts, 51 324.05
Garufi, A., Quanz, S. P., Avenhaus, H., et al. 2013, A&A, 560, A105
Guilera, O. M., Sándor, Z., Ronco, M. P., Venturini, J., & Miller Bertolami, M. M. 2020, A&A, 642, A140
Guilloteau, S., Reboussin, L., Dutrey, A., et al. 2016, A&A, 592, A124
Hildebrand, R. H. 1983, QJRAS, 24, 267
Huang, J., Andrews, S. M., Pérez, L. M., et al. 2018a, ApJ, 869, L43
Huang, J., Andrews, S. M., Dullemond, C. P., et al. 2018b, ApJ, 869, L42
Johansen, A., Blum, J., Tanaka, H., et al. 2014, Protostars and Planets VI (Tucson, AZ: Univ. Arizona Press), 547
Jørgensen, J. K., Bourke, T. L., Myers, P. C., et al. 2007, ApJ, 659, 479
Le Gal, R., Öberg, K. I., Loomis, R. A., Pegues, J., & Bergner, J. B. 2019, ApJ, 876, 72
Liu, H. B. 2019, ApJL, 877, L22
Long, F., Herczeg, G. J., Harsono, D., et al. 2019, ApJ, 882, 49
Macias, E., Guerra-Alvarado, O., Carrasco-Gonzalez, C., et al. 2021, A&A, 648, A33
Macías, E., Espaillat, C. C., Ribas, Á., et al. 2018, ApJ, 865, 37
Marino, S., Perez, S., & Casassus, S. 2015, ApJL, 798, L44
Matrà, L., MacGregor, M. A., Kalas, P., et al. 2017, ApJ, 842, 9
Maucó, K., Olofsson, J., Canovas, H., et al. 2020, MNRAS, 492, 1531
McMullin, J. P., Waters, B., Schiebel, D., Young, W., & Golap, K. 2007, ASP Conf. Ser., 376, Astronomical Data Analysis Software and Systems XVI, ed. R. A. Shaw, F. Hill, & D. J. Bell,, 127
Miyake, K., & Nakagawa, Y. 1993, Icar, 106, 20
Natta, A., Testi, L., Muzerolle, J., et al. 2004, A&A, 424, 603
Norfolk, B. J., Maddison, S. T., Pinte, C., et al. 2021, MNRAS, 502, 5779
Owen, J. E., & Clarke, C. J. 2012, MNRAS, 426, L96
Pérez, L. M., Carpenter, J. M., Chandler, C. J., et al. 2012, ApJL, 760, L17
Pérez, L. M., Chandler, C. J., Isella, A., et al. 2015, ApJ, 813, 41
Pérez, L. M., Benisty, M., Andrews, S. M., et al. 2018, ApJL, 869, L50
Phuong, N. T., Chapillon, E., Majumdar, L., et al. 2018, A&A, 616, L5
Pinilla, P., Benisty, M., Cazzoletti, P., et al. 2019, ApJ, 878, 16
Pinilla, P., Klarmann, L., Birnstiel, T., et al. 2016, A&A, 585, A35
Pinilla, P., Benisty, M., Birnstiel, T., et al. 2014, A&A, 564, A51
Pinilla, P., de Boer, J., Benisty, M., et al. 2015a, A&A, 584, L4
Pinilla, P., van der Marel, N., Pérez, L. M., et al. 2015b, A&A, 584, A16
Pinilla, P., Tazzari, M., Pascucci, I., et al. 2018, ApJ, 859, 32
Pinilla, P., Kurtovic, N. T., Benisty, M., et al. 2021, A&A, 649, A122
Powell, D., Murray-Clay, R., Pérez, L. M., Schlichting, H. E., & Rosenthal, M. 2019, ApJ, 878, 116
Ribas, Á., Bouy, H., Merín, B., et al. 2016, MNRAS, 458, 1029
Rice, W. K. M., Armitage, P. J., Wood, K., & Lodato, G. 2006, MNRAS, 373, 1619
Romero, G. A., Schreiber, M. R., Cieza, L. A., et al. 2012, ApJ, 749, 79
Sierra, A., & Lizano, S. 2020, ApJ, 892, 136
Sierra, A., Lizano, S., Macías, E., et al. 2019, ApJ, 876, 7
Sierra, A., Pérez, L. M., Zhang, K., et al. 2021, ApJS, 257, 14
Soon, K.-L., Hanawa, T., Muto, T., Tsukagoshi, T., & Momose, M. 2017, PASJ, 69, 34
Stammler, S. M., Drążkowska, J., Birnstiel, T., et al. 2019, ApJL, 884, L5
Taki, T., Fujimoto, M., & Ida, S. 2016, A&A, 591, A86
Tazzari, M., Testi, L., Natta, A., et al. 2021, MNRAS, 506, 5117
Teague, R., Henning, T., Guilloteau, S., et al. 2018, ApJ, 864, 133
Testi, L., Natta, A., Shepherd, D. S., & Wilner, D. J. 2003, A&A, 403, 323
Tsukagoshi, T., Nomura, H., Muto, T., et al. 2016, ApJL, 829, L35
Tsukagoshi, T., Momose, M., Kitamura, Y., et al. 2019, ApJ, 871, 5
Ubach, C., Maddison, S. T., Wright, C. M., et al. 2012, MNRAS, 425, 3137
Ubach, C., Maddison, S. T., Wright, C. M., et al. 2017, MNRAS, 466, 4083
van der Marel, N., Pinilla, P., Tobin, J., et al. 2015, ApJ, 810, L7
van der Marel, N., van Dishoeck, E. F., Bruderer, S., et al. 2016, A&A, 585, A58
van der Marel, N., Williams, J. P., Ansdell, M., et al. 2018, ApJ, 854, 177
van der Marel, N., Birnstiel, T., Garufi, A., et al. 2021, AJ, 161, 33
van der Walt, S., Colbert, S. C., & Varoquaux, G. 2011, CSE, 13, 22
Weidenschilling, S. J. 1977, Ap&SS, 51, 153
Williams, J. P., & Cieza, L. A. 2011, ARA&A, 49, 67
Zhu, Z., Hartmann, L., Nelson, R. P., & Gammie, C. F. 2011, ApJ, 746, 110
Zhu, Z., Zhang, S., Jiang, Y.-F., et al. 2019, ApJL, 877, L18